Cusp-artifacts in high order Superresolution Optical Fluctuation Imaging

XIYU YI[1,*] AND SHIMON WEISS[1, 2, 3,4,+]

[1]Department of Chemistry and Biochemistry, 2Department of Physiology, 3California NanoSystems Institute, University of California, Los Angeles, 90095, USA
 4Department of Physics, Institute for Nanotechnology and Advanced Materials, Bar-Ilan University, Ramat-Gan, 52900, Israel
*xiyu.yi@gmail.com, +sweiss@chem.ucla.edu

Abstract: Superresolution Optical Fluctuation Imaging (SOFI) offers a simple and affordable alternative to the more sophisticated (and expensive) super-resolution imaging techniques such as STED, PALM, STORM, structured illumination, and other derivative methods. In SOFI, the calculation of high order cumulants provides higher resolution but drastically expands the dynamic range of the resulting image. In this study, we have identified another type of artifact for high order SOFI cumulants, dubbed as 'cusp artifacts.' A series of realistic simulations are performed to study the cusp artifacts under the influences of various factors, including the blinking statistics, the spatial distribution of photophysical properties of the sample, the total number of frames processed per dataset, photobleaching, and noise. Experiments, simulations, and theory all show that high order cumulants and odd-order moments could suffer from cusp artifacts. These cusp artifacts also degrade the fidelity of bSOFI that has been proposed to solve the dynamic range expansion of image pixel intensities. Alternatively, cusp-artifacts could be altogether eliminated by utilizing even-order moments constructed directly or from cumulants for image reconstruction. Together with dynamic range compression, these approaches yield improved SOFI images. Our study provides new insight into the nature of high order SOFI images, outlines guidelines for developing and screening SOFI-optimized fluorescence probes, and suggests improved strategies for SOFI data acquisition.

1. Introduction

Super-resolution (SR) imaging techniques such as STED[1], PALM[2] SIM[3], and STORM[4] and many derivatives thereof have gained great prominence in recent years[5-8]. Super-resolution optical fluctuation imaging SOFI[9] offers an alternative and affordable approach to these methods. In SOFI, consecutive frames are acquired to form a movie of a sample labeled with stochastically blinking probes. Auto- and cross-correlation of the time trajectories of pixel intensities are then calculated, and further utilized to construct the cumulants of different orders to yield high order SOFI images. Since SOFI does not require a special hardware, and its power lies in its simple mathematical algorithm, it has the potential to 'democratize' SR imaging. The only requirement of SOFI is for the fluorescence probes to exhibit stochastic blinking at a rate that can be captured by the camera. Quantum dots (QDs)[9], organic fluorophores (dyes)[10], fluorescence proteins[11, 12], carbon nanodots[13], and Raman probes coupled to plasmonic nanoparticles[14] have been used for SOFI so far. Other forms of optical fluctuations have also been exploited for SR imaging using SOFI, such as diffusion-assisted Forster resonance energy transfer[15], protein-protein interactions (RefSOFI[16]) and diffusion of non-blinking probes (fcsSOFI[17]). The large variety of probes and implementations of SOFI suggests that SOFI could be useful for a large variety of applications.

The resolution enhancement of SOFI is manifested by the reduced width of the point spread function (PSF) in the reconstructed SOFI image. Theoretically, the PSF width for n^{th} order

SOFI image is reduced by a factor of $n^{1/2}$ as compared to the PSF in the original acquisition. Once combined with deconvolution or Fourier re-weighting[18] with an estimation of the system's optical PSF[18], an additional enhancement factor of $n^{1/2}$ can be gained, bringing the total theoretical resolution enhancement factor to n. In principle, the resolution could be further improved by increasing the SOFI order n.

However, the practical resolution enhancement of high order SOFI is limited by two fundamental issues. The first issue is the non-linear expansion of the dynamic range of pixel intensities in high order SOFI images. This expansion of the dynamic range renders the fine details in the SOFI image imperceptible. The balanced SOFI (bSOFI[19]) method has been developed and widely adopted[20] to solve the first problem by calculating the balanced cumulants, which compensate for the expanded dynamic range of pixel intensities in the high order SOFI images. However, the application of bSOFI to involve cumulants of high orders (>4) has been rarely reported, and often result with artifacts in practice. The second issue, which is often overseen in the past and is identified in this study, is resultant from the positive and negative oscillations of cumulants (Fig. 1). To be specific, the boundaries between the negative and positive regions yield artifacts (we dub as the 'cusp-artifacts') in the SOFI reconstruction. We identify the cusp-artifacts to be intrinsic to high order SOFI cumulants because it is caused by the fact that the blinking profiles of adjacent probes are inhomogeneous and finite. Further post-processing steps that rely on the high order SOFI cumulants can be negatively impacted by these artifacts, such as deconvolution algorithms with positivity constraints (as in MATLAB's 'deconvlucy' and 'deconvblind'), and high-order bSOFI reconstruction which further relies on the deconvolution performance.

We have identified the cusp-artifacts in experimental data and analyzed it through mathematical proof and simulations under various conditions that yield insights about the artifacts, which further provide guidelines for avoiding the artifacts. Since cusp-artifacts are most pronounced for high order cumulant reconstruction, exactly where dynamic range expansion degrades the reconstructed image quality, we used a cusp-artifact independent method to compress the expanded dynamic range of pixel intensities (dubbed ldrc-SOFI[22]) and compared our results to bSOFI reconstructions. Theory, simulations and analysis of experimental data all show that the bSOFI algorithm fails to faithfully reconstruct the true image at high orders as influenced by the cusp-artifacts. Besides, the susceptibility of moments reconstruction as compared to cumulants reconstruction are examined in this work. We find out that even-orders moments are immune to cusp-artifacts, and tend to smooth the features-of-interest while still maintaining some degree of resolution enhancement (over the diffraction limit), therefore, it has the potential to be a practical (but mathematically non-rigorous) solution to circumvent the cusp-artifacts. When compared to bSOFI, even-order moments treated by ldrc-SOFI yield much more faithful images up to 6th order. More detailed examinations are available in our accompanying manuscript[22], where both theoretical and experimental demonstrations show that it is possible to avoid cusp-artifacts by choosing an even-order-moments reconstruction as a short-term solution for eliminating cusp artifacts.

The work described here is organized as follows: in section 2 we briefly review the SOFI theory. Section 3 introduces the mathematical concept of 'virtual-emitters' and 'virtual-PSF' for high order SOFI images (to be used in the following sections). Section 4 presents the theoretical explanation for the cusp-artifact. Section 5 examines the conditions that yield cusp-artifacts. Section 6 examines the ill-effects of cusp-artifacts on balanced cumulants and on deconvolution post-processing algorithms. We discussed that cusps-artifacts could be altogether eliminated by utilizing even-order moments (instead of cumulants) for image reconstruction. Section 7 compares the performance of the various algorithms on real data. We conclude by discussing the implications of our findings in sections 8 and 9.

2. A review of SOFI's theory

One of the most common SOFI super-resolution image reconstruction is performed on a stack of frames (a movie) acquired with a simple wide-field imaging system. The sample is labeled with stochastically blinking probes. Each point emitter (probe) in the sample plane is imaged onto the camera plane via the optical imaging system, and due to the diffraction limit of light, its intensity distribution takes the shape of the point-spread function (PSF). The signal captured at a given camera's pixel located at $\vec{r}$ can be expressed as follows (excluding binning effects due to pixilation):

$$F(\vec{r},t) = \sum_{k=1}^{N} \epsilon_k b_k(t) U(\vec{r} - \vec{r}_k) , \qquad (2.1)$$

where $\vec{r}$ is the location of the pixel in the imaging plane, N is the total number of emitters, k is the emitter index, $\vec{r}_k$ is the location of the kth emitter, ϵ_k is the brightness of the k emitter when it is in the 'on' state, and $b_k(t)$ is the blinking time trajectory of the kth emitter. $b_k(t) = 1$ when the emitter is in the 'on' state, and $b_k(t) = 0$ when the emitter is in the 'off' state. $U(\vec{r})$ is the PSF of the imaging system that is determined by the optical setup as well as the emission wavelength of the emitters.

In SOFI, temporal average of each pixel's time trajectory is subtracted from the signal, such that only the fluctuations (around zero) are considered:

$$\delta F(\vec{r},t) = F(\vec{r}) - \langle F(\vec{r}) \rangle_t = \sum_{k=1}^{N} \epsilon_k \delta b_k(t) U(\vec{r} - \vec{r}_k) , \qquad (2.2)$$

where $<>_t$ represents the time average operator, and $\delta b_k(t)$ represents the fluctuation of blinking trajectory $b_k(t)$. The cumulants of $\delta F(\vec{r},t)$ are then calculated. In the case of 2nd order, the cumulant (C_2) is equivalence to correlation function:

$$C_2(\tau) = \langle \delta F(\vec{r},t) \delta F(\vec{r},t+\tau) \rangle_t = \sum_{k=1}^{N} \sum_{j=1}^{N} \epsilon_k \epsilon_j \langle \delta b_k(t) \delta b_j(t+\tau) \rangle_t U(\vec{r} - \vec{r}_k) U(\vec{r} - \vec{r}_j) \qquad (2.3)$$

Assuming that the emitters blink independently, the temporal cross-correlation between blinking trajectories of two emitters is zero. Only the auto-correlation of a single emitter trajectory with itself yields non-zero values:

$$\langle \delta b_k(t) \delta b_j(t+\tau) \rangle_t \begin{cases} =0, & \text{for } k \neq j \\ \neq 0, & \text{for } k=j \end{cases} \qquad (2.4)$$

So equation (2.3) becomes:

$$C_2(\tau) = \sum_{k=1}^{N} \epsilon_k^2 \omega_{2,k}(\tau) U^2(\vec{r} - \vec{r}_k) , \qquad (2.5)$$

where $\omega_{2,k}(\tau)$ is the second order cumulant of $\delta b_k(t)$. The derivation above can be extended to higher order cumulants[23]. Noticing that cumulants are additive[23], the nth order cumulant of $\delta F(\vec{r},t)$ could be expressed as the sum of cumulants of individual emitters:

$$C_n(\vec{r}, \tau_1, ..., \tau_{n-1}) = \sum_{k=1}^{N} \epsilon_k^n \omega_{n,k}(\tau_1, \tau_2, ..., \tau_{n-1}) U^n(\vec{r} - \vec{r}_k) \qquad (2.6)$$

Where $\omega_{n,k}(\tau_1, \tau_2, ..., \tau_{n-1})$ is the nth order cumulant of $\delta b_k(t)$, and can be simplified as $C_n[\delta b_k(t)]$ when the time lags are not specified.

3. Virtual-emitters interpretation of high order SOFI

Notice the similarity between equation (2.6) (describing the nth order SOFI cumulant) and

equation (2.1) (describing the original image). Both equations share a similar format, with the term $\epsilon_k b_k(t)$ being replaced by $\epsilon_k^n \omega_{n,k}(\tau_1, \tau_2, ..., \tau_{n-1})$ and with $U(\vec{r} - \vec{r}_k)$ replaced by $U^n(\vec{r} - \vec{r}_k)$. We dub the term $\epsilon_k^n \omega_{n,k}(\tau_1, \tau_2, ..., \tau_{n-1})$ as the 'virtual brightness' of the kth 'virtual emitter', with $U^n(\vec{r} - \vec{r}_k)$ as the 'virtual PSF'.

Compared to the original emitters, the virtual emitters are located at exactly the same locations as we have in the original sample, because $\vec{r}_k$ are not changed in the function. In addition, the apparent PSF is raised to the power of n. Since the PSF could be estimated as a three dimensional Gaussian function, the width of the PSF is thus reduced by a factor of $n^{1/2}$, as illustrated below:

$$U^n(r_x, r_y, r_z) = \exp\left(-\left(\frac{r_x^2 + r_y^2}{2 \cdot (\frac{\sigma_{xy}}{\sqrt{n}})^2} + \frac{r_z^2}{2 \cdot (\frac{\sigma_z}{\sqrt{n}})^2}\right)\right) \tag{3.1}$$

where σ_{xy} and σ_z are the respective widths of the original PSF in the xy- and z-plane. The reduction of apparent PSF widths provides the basis for resolution enhancement in SOFI cumulants (in all three dimensions).

In order to better understand and describe the physical meaning of SOFI cumulants, we introduced above the concept of 'virtual-emitters' having 'virtual brightnesses' and reduced-size 'virtual PSF'. In the nth order SOFI image, the virtual brightness of the kth virtual emitter includes the on-state brightness factor ϵ_k raised to the power of n. This is the factor responsible for the dynamic range expansion of the resulting SOFI image. It also includes a second factor that resembles the time dependent blinking profile $b_k(t)$ in the original image, but now changed into $\omega_{n,k}(\tau_1, \tau_2, ..., \tau_{n-1})$, where $\omega_{n,k}$ is the nth order cumulant of the blinking time trajectory's fluctuation $\delta b_k(t)$. The locations of emitters are unchanged in the cumulant image as compared to the original image.

The virtual-emitters interpretation of SOFI would thus be: for a given order of SOFI cumulant, the resulting image is equivalent to an image captured with a virtual microscope that has a virtual PSF with reduced width compared to the original PSF (i.e. with increased resolution), and the captured signal is formed from virtual emitters that are located at exactly the same location as the real emitters in the sample, but with virtual brightness's that differ from the real emitter brightness and could exhibit either positive or negative values.

We will demonstrate in the following section that $\omega_{n,k}(\tau_1, \tau_2, ..., \tau_{n-1})$ has positive and negative oscillations with respect to different blinking behavior of emitters, and is responsible for cusp-artifacts in high-order SOFI images.

4. The origin of cusp-artifacts

Let's assume a two-state blinking profile $b(t)$ for the real emitters with $b(t) = 1$ indicating the 'on' state and $b(t) = 0$ indicating the 'off' state. Let's define ρ_k as the fraction of time that the emitter spends in the 'on' state during the total duration of signal acquisition (ρ_k 'on-time ratio'). If the acquisition time is long enough, and if the blinking behavior can be statistically described by a Poisson process, ρ_k would converge to:

$$\rho = \frac{\tau_{on}}{\tau_{off} + \tau_{on}} \tag{4.1}$$

For a pure power-law blinking statistics, ρ_k will not converge[24]. Adjacent emitters could have different ρ_k values (in principle) due to: (i) finite acquisition time (i.e. not reaching statistical

significance to represent the underlying statistical process); (ii) subtle changes in local microenvironments; (iii) inhomogeneity in photophysical properties (as for example, in quantum dots). Any order of $b_k(t)$ cumulants can be expressed as a function of ρ_k. If, for simplicity, we set all the time lags equal to zero, we find that the cumulants with order higher than 2 will have positive-negative oscillations as function of the on-time ratio ρ_k. Formulas (detailed derivation is given in Supplementary Note 1) for the first 6 cumulants (2nd order to 7th order) as functions of ρ_k are given by:

$$\omega_2(\rho) = \rho - \rho^2$$
$$\omega_3(\rho) = \rho - 3\rho^2 + 2\rho^3$$
$$\omega_4(\rho) = \rho - 7\rho^2 + 12\rho^3 - 6\rho^4$$
$$\omega_5(\rho) = \rho - 15\rho^2 + 50\rho^3 - 60\rho^4 + 24\rho^5 \tag{4.2}$$
$$\omega_6(\rho) = \rho - 31\rho^2 + 180\rho^3 - 390\rho^4 + 360\rho^5 - 120\rho^6$$
$$\omega_7(\rho) = \rho - 63\rho^2 + 602\rho^3 - 2100\rho^4 + 3360\rho^5 - 2520\rho^6 + 720\rho^7$$

where the emitter index k and the time lags (τ_1, ..., τ_{n-1}) are eliminated to simplify the notation.
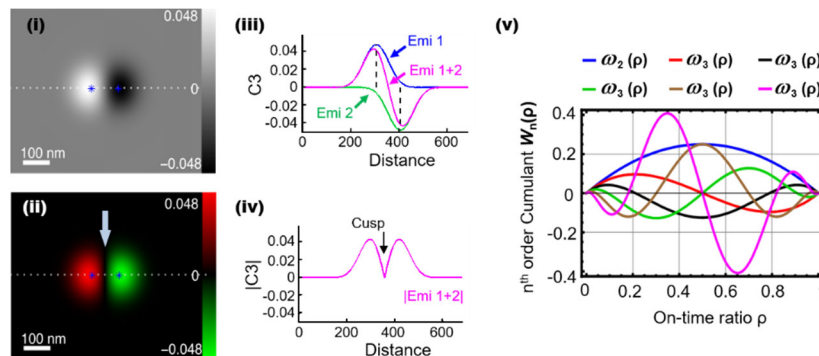

Fig. 1. Demonstration of cusp artifact. Panels (i) and (ii) show two representations of the same theoretical 3rd order SOFI cumulant image of two emitters. (i) shows a gray scale display, while (ii) shows a g/r color code with red representing positive cumulant values and green representing negative cumulant values, both with a dynamic range of -0.048 to 0.048. The on-time ratio of the left emitter was set to 0.4 and of the right emitter to 0.6. Panels (iii) and (iv) show cross-sections plots at the dashed line in (i) and (ii) respectively. Panel (v) shows plots of cumulants ω_n as a function of ρ, with n = 2 to 7. All the cumulants (n > 2) oscillate between negative and positive values with number of zero crossings equal to n-2. As can be seen, $\omega_3(0.4) > 0$ and $\omega_3(0.6) < 0$, corresponding to the virtual brightnesses shown in (i) and (ii). The cusp artifact for this example is highlighted by an arrow in (iv).

Fig. 1v shows different cumulants orders as functions of the on-time ratio ρ. High orders (> 2nd) clearly exhibit sign oscillations. If the virtual brightnesses of two near-by virtual emitters have opposite signs (Fig. 1i and Fig. 1ii), the corresponding amplitude cross-section of the SOFI amplitude image (consisting of the convolution of the virtual emitters with the virtual PSF) will exhibit positive and negative lobes (Fig. 1iii). The absolute value of this cross-section (a common step in displaying an image) exhibits a cusp (Fig. 1iv, arrow). We therefore dub this artifact as the 'cusp-artifact'.

In order to better demonstrate the cusp-artifact, we performed simulations for 3 adjacent blinking emitters with the same on-state brightness, but with on-time ratios of 0.831, 0.416, and 0.103 respectively (Fig. 2). The simulations clearly show that high order cumulants can take negative values that coexist with positive values, leading to cusp-artifacts.
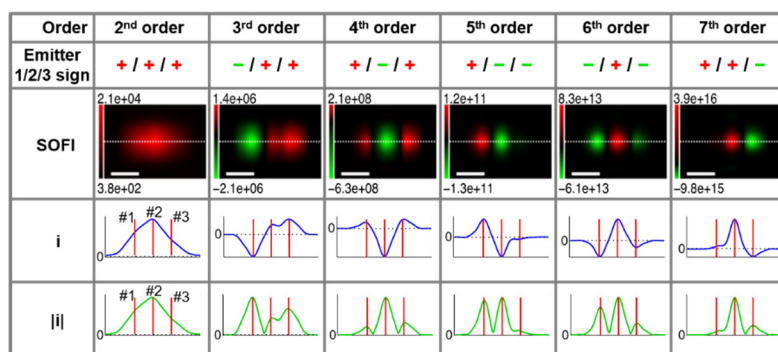
Fig. 2. Demonstration (by simulations) of cusp artifacts for 3 near-by blinking emitters that are equally spaced along a line (193 nm spacing between nearest neighbors). The simulated parameters are: emission wavelength - 800nm; numerical aperture NA=1.4; pixel size - 93.33 nm. For blinking statistics (simulated by Monte Carlo), we set ρ to 0.831, 0.416, and 0.103 for emitters 1, 2, and 3 respectively. The orders of the cumulants are labeled at the top row. Signs of the virtual brightness, as predicted by Fig. 1v, are denoted by (+/-) signs (second row). The third row shows simulated SOFI images for cumulant order 2 to order 7 (left to right). The fourth row (i) shows cross sections for dotted white line in the second row (in blue; red line denotes emitters positions). The fifth row shows the absolute value cross sections of |i| for dotted white line in the second row (in green; red line denotes emitters positions). Sign oscillations and cusp artifacts are evident except for order 2. Scale bars: 280nm.

Moreover, when displaying gamma corrected[25] experimental high-order SOFI-processed images (before applying deconvolution or Fourier re-weighting), cusp artifacts are readily observed for orders >2, as can be seen for the gray/red boundaries in Fig. 3.
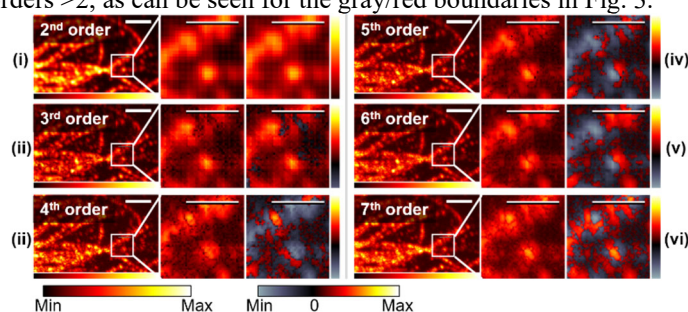

Fig. 3. Gamma-corrected high-order SOFI-processed experimental images displaying cusp artifacts. Fixed Hela cells were labeled with quantum dots (emission wavelength = 800 nm) by immuno-staining using primary antibody (eBioscience, Cat#: 14-4502-80) and secondary antibody conjugated to QD800 (ThermoFinsher Scientific. Ref#: Q11071MP). 2000 frames (30 ms exposure time) were processed to get SOFI cumulants up to 7th order using both auto- and cross-correlations. In order to better illustrate the source of cusp artifacts, the final SOFI processing steps of deconvolution and Fourier re-weighting were skipped. Each SOFI order image is presented in 3 panels: large field-of-view (left), absolute value SOFI image zoom-in to box area (middle) and positive/negative values SOFI image zoom-in to box area (right). Positive/negative domains are color coded separately as shown by the color bars for each panel with the color scheme shown in the bottom. Cusp artifacts are clearly seen for cumulants of order > 2: The spatial distribution of cusps differs between different cumulants orders, and they are located at the boundaries between positive and negative domains. Scale bars: 3.2 μm (left) and 1.6 μm (middle/right).

5. Exploration of cusp-artifacts' parameter space

In order to better understand the prevalence and significance of cusp-artifacts in SOFI reconstructions, we performed a series of realistic simulations that explore the relevant parameter space. A simulator was developed that propagates point emitters in the sample plane

onto the detector (camera) plane using the Gibson Lanni's PSF model[26]. Point emitters' emission trajectories were simulated to blink according to Poisson statistics. Poisson noise was simulated as described in our accompanying manuscript[22]. Real experimental background noise was recorded by an EMCCD camera and added to the simulated movie. SOFI cumulants up to 7th orders were then calculated and analyzed. Long (20,000 frames) simulations were performed to ensure good statistical significance of the blinking trajectories. More details describing the simulator are discussed in our accompanying manuscript[22] and posted on a public GitHub package as SR_Simu3D[27].
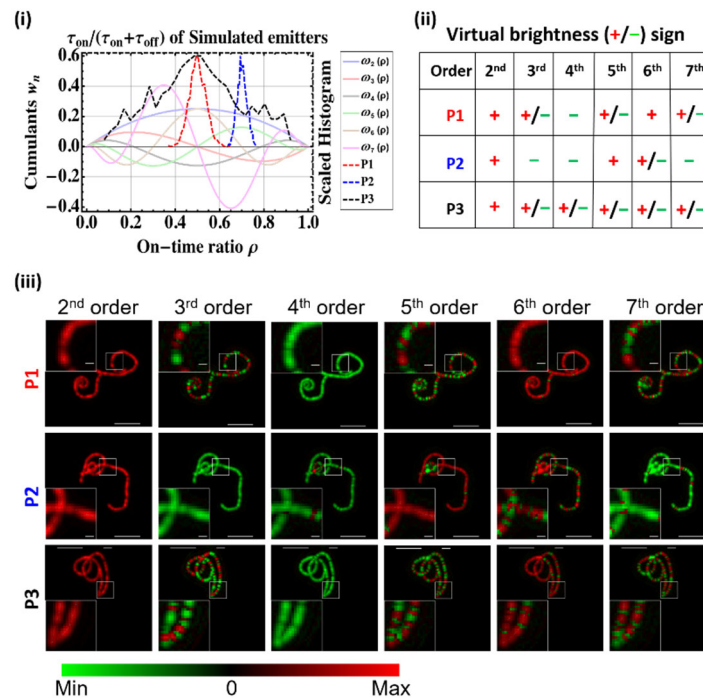

Fig. 4. Simulations ('Simulation-1') showing cusp-artifacts dependence on blinking statistics. (i) Three different populations of simulated emitters with different distributions of τ_{on} and τ_{off} values, yielding three different distributions of ρ values P1, P2 and P3 (dashed red, blue, and black curves respectively) are plotted on top of Fig. 1v. (ii) Predictions for the signs of the resulted virtual brightnesses for P1, P2 and P3 for cumulants orders 2 to 7. (iii) SOFI processing of the simulated data. A simulated filamentous morphology was populated with emitters from either P1, P2 or P3. Signs of virtual brightnesses (red for positive, green for negative) of virtual emitters mostly follow the predictions in (ii) for the different orders, except for out-of-focus (P2) regions (details are given in Supplementary Note 2).

In the first set of simulations ('simulation-1'), we simulated three different populations of emitters (P1, P2 and P3) with different ρ distributions (Fig. 4i, dashed red, blue, and black curves) with the ranges of $0.49 \leq \rho \leq 0.51$ for P1, $0.53 \leq \rho \leq 0.87$ for P2 and $0.11 \leq \rho \leq 0.93$ for P3 (Fig. 4i). Comparing these distributions to Fig. 1v allowed us to predict the signs of resulted virtual brightnesses (Fig. 4ii). A simulated filamentous morphology was then populated with emitters from either P1, P2 or P3 populations. And the resulting simulated movies were SOFI-processed up to 7th order. Signs of virtual brightnesses of virtual emitters (defined in section 3) mostly follow the predictions in Fig. 4ii for the different orders, except for out-of-focus P2 emitters regions (details are given in Fig. S1). As we can see from Fig. 4i, for P1, ρ is distributed in a region with positive lobes for 2nd and 6th order cumulants, negative lobe for 4th order cumulant, and positive/negative transition regions for 3rd, 5th and 7th order cumulants. This means that all P1 virtual emitters will exhibit positive virtual brightnesses for

2nd and 6th order cumulants, negative virtual brightnesses for the 4th order cumulant, and exhibit both negative and positive virtual brightness in the 3rd, 5th and 7th order cumulants. We could therefore predict that P1 would exhibit cusp-artifacts for 3rd, 5th and 7th cumulants orders. Similarly, for P2, ρ is distributed in a region with positive lobes for 2nd and 5th order cumulants, negative lobes for 3rd, 4th and 7th order cumulants, and positive/negative transition regions for 6th order cumulants. We could therefore predict cusp-artifacts for cumulants of 6th order for P2. For P3, ρ is broadly distributed at positive/negative transition regions for all cumulants with orders higher than 2, and is purely positive only for 2nd order cumulant. P3 is therefore predicted to exhibit cusp-artifact for all cumulants with orders higher than 2. This prediction is clearly validated in Fig. 4iii except for the 4th order cumulant. The reason the 4th order cumulant exhibit only negative virtual brightnesses is because the portion of positive virtual emitters is too small as compared to the negative portion, the signal is canceled out and couldn't stand out from the large portion of positive signals.

We assumed in our simulation that the blinking is governed by a Poisson process, i.e. the photon emission from an individual emitter assumes a telegraph noise-like time trajectory. If enough data (a large number of movie frames) with sufficient statistical significance is collected, the estimator for the 'on'-time ratio ρ would converge to $\tau_{on} / (\tau_{on} + \tau_{off})$ (Equation (4.1)). As the total number of frames in the simulation is reduced, the actual (calculated) value of ρ starts to deviate from its estimated value. This could lead to unexpected cusp-artifacts in certain cumulant orders, in regions that are predicted to be cusp-artifact free. Supplementary Note 2 shows that the higher the SOFI order, the more frames are needed for SOFI processing to reach the theoretical prediction of cusp-artifact-free images. Moreover, since high order virtual brightnesses exhibit more sign oscillations, they are more susceptible to heterogeneities in photo-physical properties and hence more vulnerable to cusp-artifacts.

The next set of simulations ('simulation-2') examines the effects of photobleaching and noise on cusp-artifacts (Fig. 5). Time trajectories that were simulated in simulation-1 from P1 were stochastically truncated (using Poisson bleaching statistics) to simulate the bleaching events (see Supplementary Note 3 and Fig. 5i - iii). The predicted signs of virtual brightnesses of emitters in P1 are labeled on top of the first row of Fig. 5iv. As can be seen in the first row of Fig. 5iv where there is no bleaching correction (see below), the virtual brightness signs displayed in the SOFI images deviate from the predictions. This is because bleaching alters ρ away from its estimated value (Equation (4.1)) as the "bleached" state is equivalence to an ultra-long 'off' state, leading to reduced ρ values in emitters. This drives the predicted virtual emitter signs away from the theoretical predictions (4.1). The 'bleached' state also affects the independency assumption of blinking trajectories between different emitters, rendering the prediction less reliable. We then applied a bleaching correction algorithm[14] with minor modifications (Supplementary Note 3) to the simulated data by dividing the whole movie into individual blocks of frames, where each block has a signal decrease (from beginning to end of block) of f_{bc} = 1% of the overall signal decrease (from beginning to end of the whole movie; f_{bc} is dubbed as the 'bleaching correction factor'). The final cumulant reconstruction is computed as the average of the cumulants of all time blocks of (and same order). We can see that bleaching-corrected reconstructions (second row of Figure 5iv) restore the predicted virtual brightness signs. We then examined the effect of SNR on the bleaching correction. EMCCD camera noise was recorded and added to the simulated bleaching data with altered signal levels (as described in Supplementary Note 3.2), to reach SNR levels of 1.47 (third row) and -1.33 (bottom row). The resulting simulations with bleaching and background noise are SOFI processed up to 7th order. As can be seen, the noise severely degrades the quality of the images, especially for the cumulant orders with large portion of positive virtual emitters. Interestingly, if the emitters' blinking parameters could be tuned to yield pure negative virtual brightnesses

(as shown for the 4th order cumulant in the third row), a large contrast enhancement could be achieved (as shown for this set of simulations). On the other hand, if large portion of the virtual emitters are negative, the negative portion could still create high contrast as a negative contrast against the positive noise background (as shown for the 7th order cumulant in the third and fourth row). We note here that cumulants of background noise are positive for all cumulant orders higher than 2, this is because high order (>2) cumulants of a random variable that follows a Poisson distribution are constant (Supplementary Note 4).
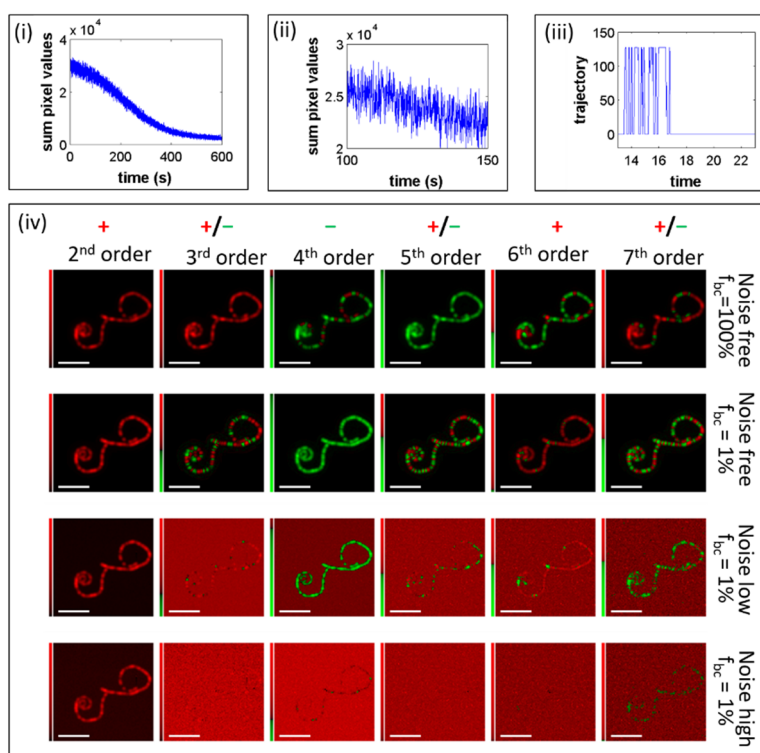

Fig. 5. Simulations ('Simulation-2') assessing the contributions of bleaching and noise to cusp-artifacts. (i) Total signal, summed over all pixels, as function of movie frame (time), after the bleaching operator is implemented (before adding background noise). (ii) A temporal zoom-in to the curve in (i), showing intensity fluctuations. (iii) An example for a single emitter blinking trajectory that was 'bleached' around ~17 s. (iv) An array of SOFI cumulants images and as function of noise, for orders 2nd to 7th. Top row shows simulated images with no bleaching. The sign of virtual brightness follows predictions according to Fig. 4i (bleaching correction factor fbc = 100% means no bleaching correction). Second row shows simulated images for a bleaching correction factor of fbc = 1% (see text). The bleaching correction algorithm is effective in restoring the absolute value of the virtual brightness distribution, but not their signs. The bleaching correction protocol alters the signs of the cumulants and results in rapid sign changes in 3rd, 5th, and 7th odd orders. Real background noise (recorded with an EMCCD camera as empty frames) is added to the simulated bleaching data severely degrades the quality of the images (background noise is always positive). If the emitters' blinking statistics yields pure negative virtual brightnesses, as shown for the 4th order cumulant in the third row, a large contrast enhancement is resulted.

We emphasize here the trade-offs between bleaching correction factor f_{bc}, noise level and statistical significance of blinking trajectories (details available in Supplementary Note 3). When we decrease f_{bc}, the block size decreases, and the total number of bleaching events happened within each block decreases, so the bleaching effect is better suppressed. However, because decreased f_{bc} leads to decreased distinctness between blinking events and noise within

each block, the cumulants construction becomes more vulnerable to noise. In addition, smaller f_{bc} leads to decreased statistical significance of blinking trajectories within each block, as well as increased total number of blocks for the final cumulant construction, these two factors counterbalancing each other on the influence of f_{bc} on the overall statistical significance of blinking trajectories.

In the simulations discussed above (simulation-1 and simulation-2), the spatial distribution of different emitters' ρ is random. In Fig. 6 we explore another set of simulation ('simulation-3') in which the ρ values are slowly-varying across the spatial field of view, and SOFI cumulants of 2nd to 7th orders are calculated. As can be seen, the number of zero crossing nodes is increased with cumulants order and the spatial variation of blinking statistics is visually seen as green/red segments (with the cusps serving as segments boundaries).
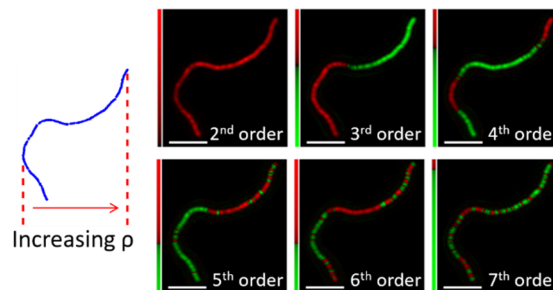

Fig. 6. Simulations ('Simulation-3') assessing the dependence of cusps-artifacts on slowly varying ρ. Different orders of cumulant are displayed with gamma scale (gamma = 1/n). Color coding are shown as bars to the left of each panel (green for negative values, red for positive values, black for 0). Emitters are positioned along the feature of interest (filament) with a spatially varying ρ (leftmost panel). The number of zero crossings (green/red transitions) is increased with cumulants order along the gradient of ρ values.

To summarize this part: mixed populations of positive and negative virtual brightnesses cause Cusp artifact. Information of virtual brightness distribution based on the blinking statistics can yield prediction of the cusp artifact. SOFI cumulants that intrinsically have cusp artifacts are more vulnerable to the background noise because of the lowered virtual signal amplitude due to neutralization between positive and negative virtual brightnesses and attenuation by small amplitudes of cumulant w_n. Bleaching effect affects the prediction of cusp-artifact, but bleaching correction can diminish this effect and restores the validity of the cusp-artifact prediction. Too small of an f_{bc} will make the SOFI cumulants more vulnerable to background noise (especially when the cumulant order is high) but doesn't have significant effect on the statistical significance of blinking trajectories. Lastly and interestingly, in the ideal cases where the spatial variation of blinking statistics is very small, cusps can serve as the boundaries to segments with similar blinking statistics (with the segment, but different blinking statistics between segments).

6. Effects of cusp-artifacts on image deconvolution and dynamic-range expansion correction, and moment alternative

We have shown in previous sections that spatial variations in the 'on' time ratio ρ could lead to positive/negative-value variations in cumulants, which in turn produce cusp-artifacts after applying the absolute value operator to the calculated cumulants images. Subsequent steps in the SOFI protocol include deconvolution (and / or Fourier re-weighting)[18] and dynamic-range expansion correction (bSOFI[19], or *ldrc* as introduced in our accompanying manuscript[22]) to yield the final SOFI image. In this section we examine the effect of cusp-

artifact on these two subsequent ('post-processing') steps. We argue that if not handled properly, the ill-effect of cusp-artifacts could be amplified by the post-processing steps.
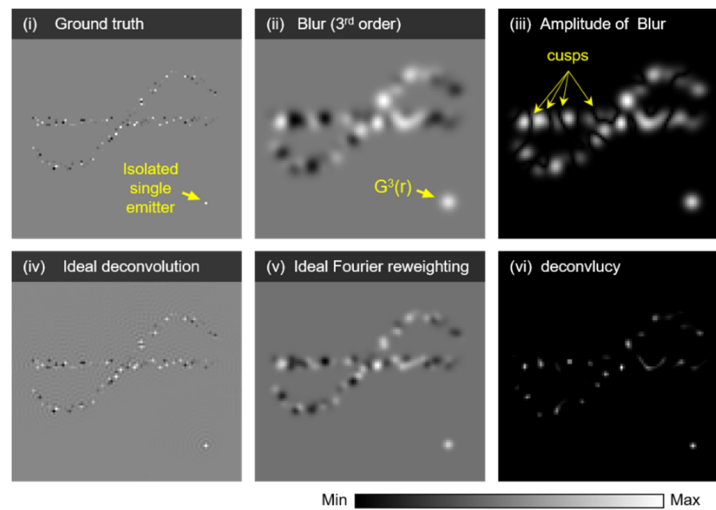

Fig. 7. Post-procession of SOFI reconstructions containing cusp artifacts (Simulation). Reconstructions amplitudes are displayed in gray scale (each panel with a different dynamic range). The background of each panel is always zero (and therefore should be used as a reference). Negative pixel values carry darker colors than the background; Positive pixel values carry lighter colors than the background. (i) the ground truth virtual emitters with both positive and negative values. (ii) the corresponding 3rd order cumulant image (convolved with the PSF). (iii) the amplitude (absolute value) of (ii) Cusps are clearly visible. (iv) ideal deconvolution result obtained by dividing the Fourier-transformed image by the optical transfer function (OTF) followed by an inverse Fourier transformation. (v) ideal Fourier-reweighting, where as compared to the case of ideal deconvolution, the Fourier spectrum is further multiplied by an extended OTF before the inverse Fourier transform. (vi) deconvolution result using deconvlucy that imposes positivity constraint. The PSF is simulated as a perfect Gaussian with a standard deviation of 4 pixels.

In order to isolate factors that contribute to imperfections, the simulations that are summarized in Fig. 7 are done for the ideal case of a collection of positive and negative virtual emitter (Fig. 7i) corresponding to a 3rd order cumulants with zero background and noise. The blurred image (Fig. 7ii) is generated by convolving the ground-truth image with the PSF. In the amplitude display (absolute value) of this image (Fig. 7iii), cusps are clearly revealed between the positive/negative regions in the image. The images are generated on fine grids without noise, diminishing the possible imperfections due to noise, pixilation, discrete Fourier transform, etc. Almost perfect deconvolution is achieved (Fig. 7iv) using direct division by the optical transfer function (OTF) in the Fourier space followed by inverse Fourier transform (despite ringing artifacts due to discrete Fourier transform). The virtual emitters are recovered with intact virtual brightnesses (including the negative ones). In the case of Fourier re-weighting (mimicking the case of 3rd order cumulants) the transformed image is divided by a modified OTF with a damping factor (we used machine epsilon variable in MATLAB, representing a small number). The Fourier spectrum is subsequently multiplied by an OTF with a wider support. This is equivalent to convolving the ground truth with a smaller Gaussian PSF (Fig. 7v). Since the signs of the virtual brightnesses are conserved the cusp artifacts are maintained at the high density regions. However, if we perform deconvolution with solvers that impose positivity constraints (for example, MATLAB's 'deconvlucy' or 'deconvblind'), deconvolution fails (Fig. 7vi). We attribute this failure to presence of negative pixel values (or image domains), and cusps. When the pixels are forced to be positive by either taking the absolute values or by rejecting all negative values, the image is no longer the result of a convolution between the PSF and the ground truth image.

In cases where a subsequent dynamic range compression step ('balancing' step in bSOFI) is performed after deconvolution, the final SOFI image can be further distorted. Note here that the current open source bSOFI package (MATLAB version[28]) uses '*deconvlucy*' that imposes positivity constraints and therefore improperly handles negative virtual brightnesses. In contrast, Fourier re-weighting does not alter the sign of virtual brightnesses but it is very sensitive to noise and it doesn't eliminate cusps.

As shown in equation (2.6) and discussed in section 2, cumulants are additive and therefore the nth order cumulant could be expressed as a sum of cumulants of individual emitters. This property is, in fact, the reason why cumulants reconstruction was originally chosen[9]. Reconstruction by moments (rather than by cumulants) were not considered due to the mixed terms that contain signal contributions from multiple individual emitters, rendering such a reconstruction mathematically not rigorous with uninterpretable physical meaning. Nonetheless, since even-order moments are intrinsically free of cusps-artifacts, we further pursued moments reconstruction as a ***practical*** approach and have shown that they still maintain enhanced resolution as compared to the diffraction limit (as shown in the accompanying moments reconstruction paper[22] and section 8).

7. Performance comparisons

We compared the performance, with respect to cusps-artifacts, of 6th order reconstructions by SOFI, bSOFI, and 6th order moments (M6) + ldrc, as shown in Fig. 8.
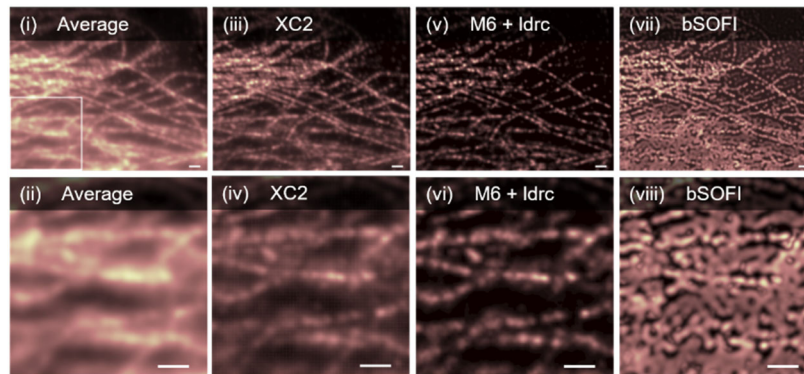

Fig. 8. QD800 labeled microtubules (experimental data). First column: (i) Average image of a movie (2000 frames, 30 ms per frame) of QD800 labeled α-tubulin in a fixed Hela cell. (ii) a zoom-in to the boxed region in sum image (i); Second column: (iii) and (iv) show 2nd order SOFI cumulants with extra pixels generated by cross-correlations (XC2), corresponding to panels (i), (ii) respectively; Third column: 6th order moments reconstruction with local dynamic range correction, corresponding to panels (i), (ii) respectively; Fourth column: 6th order bSOFI corresponding to panels (i), (ii).

All reconstructions were performed on the same data set (movie) of an α-tubulin network in a fixed Hela cell that was labeled with blinking QD800 (ThermoFisher Scientific, Carlsbad, CA). 2000 movie frames were collected at 33 Hz using an EMCCD camera (Andor USA, South Windsor, CT). Results are shown in Figure 8. Note that no deconvolution or Fourier reweighting was implemented for M6 in order to isolate the factors responsible for resolution enhancement and to asses to what degree cusps-artifacts degrade their overall performance. A more detailed performance analysis for moments reconstruction is discussed in the accompanying manuscript[22]. Note that for bSOFI reconstruction a deconvolution step was included because balanced cumulant reconstruction is a post-processing step performed after deconvolution.

Both Average, XC2, M6 + ldrc and bSOFI show faithful reconstructions at regions where filaments' density is low and α-tubulins are well separated. On the other hand, XC2 and bSOFI

performs better than M6+ldrc in terms of feature visibility. However, at regions where filaments' density is high, as shown in the boxed region in (i) and displayed in (ii), (iv), (vi), (viii) respectively, M6-ldrc out-performs the Average, XC2 and bSOFI.

8. Discussion

Cusps-artifacts have not been previously identified for several reasons: (i) 2nd order cumulants are always positive and therefore are not susceptible to these artifacts. Many SOFI works stopped at order 2. (ii) post-processing steps such as balancing and deconvolution mask the existence of cusps-artifacts and their origin. (iii) super-resolution methods in general, and SOFI and SOFI-derivatives reconstructions in particular, are an attempt to solve an ill-defined inverse problem (location of emitters in the sample). It is very hard if not impossible to identify cusps-artifacts from experimental data. It is only after we performed realistic simulations (including dark noise, read-out noise, background, out-of-focus light, and spatial variability in photophysical properties) and compared reconstruction algorithms to the ground-truth, that we were able to identify and characterize cusps-artifacts. As shown in Fig. 3, once cusps were identified, careful re-examination of experimental data did indeed confirm their existence.

Cusps-artifacts, are in fact, hard to avoid. Even if photophysical properties (blinking and photobleaching) of emitters are more-or-less uniform across the sample, the finite acquisition time of a SOFI experiment (usually ~2,000 to 20,000 frames) is often not long enough to reach statistical significance of blinking behavior, leading to a broad distribution in ρ values, which in turn leads to positive and negative higher order (>2) cumulants values (Figure 1). It is only when all emitters in the sample exhibit a narrow ρ distribution during the data acquisition duration that cusp-artifacts could, in principle, be avoided (as shown in Figure 4 for P1 with cumulants of 2nd , 4th and 6th orders.). However, narrow ρ distribution could still be positioned close to a zero crossing of one (or more) of the high order cumulants, leading to coexistence of positive and negative cumulants values.

To minimize ill-effects of cusps-artifacts, the following guidelines should be considered: (1) emitters with uniform photophysical parameters (blinking, bleaching) should be used to achieve an intrinsically narrow distribution of ρ; (2) long movies (with a large number of frames) should be acquired (to narrow down the experimental ρ distribution); (3) to the extent possible, ρ distribution should be tuned to a zero-crossing-free zone (see Figure 1); (4) bleaching should be minimized and bleaching correction[14] should be applied to the data set, while following guidelines (1)-(3) for each bleaching correction block.

9. Conclusions

We identified cusps-artifacts in SOFI image reconstructions of orders greater than > 2. These artifacts have been previously missed or erroneously interpreted. In this work we proposed the virtual emitter interpretation of high order SOFI cumulants, from which we derived the theoretical explanation of cusp artifacts. We performed a series of realistic simulations that provide insight into the origin of cusps-artifacts, and suggested guidelines on how to minimize their ill-effects. We demonstrated that moments reconstructions could improve, and sometimes even eliminate these artifacts. Our study also suggests guidelines for how to screen for improved probes that could minimize cusps-artifacts for high order SOFI cumulants. Additionally, under the novel theoretical framework of virtual emitter interpretation, our work provided insights of high order SOFI cumulants as well as the cusp artifacts that could potentially inspire positive utilization the abnormal virtual brightness distribution and cusps where ρ can serve as an indicator.

Author Contributions

S. W. and X. Y. designed the research, X. Y. performed the experiments, developed simulations, the analysis methods and the associated codes, S. W. and X. Y. wrote the manuscript. These authors declare no conflict of interests.

Acknowledgement

References

1. S. W. Hell and J. Wichmann, "Breaking the diffraction resolution limit by stimulated emission: stimulated-emission-depletion fluorescence microscopy," Optics letters **19**, 780-782 (1994).
2. E. Betzig, G. H. Patterson, R. Sougrat, O. W. Lindwasser, S. Olenych, J. S. Bonifacino, M. W. Davidson, J. Lippincott-Schwartz, and H. F. Hess, "Imaging intracellular fluorescent proteins at nanometer resolution," Science **313**, 1642-1645 (2006).
3. M. G. Gustafsson, "Surpassing the lateral resolution limit by a factor of two using structured illumination microscopy," Journal of microscopy **198**, 82-87 (2000).
4. M. J. Rust, M. Bates, and X. Zhuang, "Sub-diffraction-limit imaging by stochastic optical reconstruction microscopy (STORM)," Nature methods **3**, 793 (2006).
5. A. M. Sydor, K. J. Czymmek, E. M. Puchner, and V. Mennella, "Super-resolution microscopy: from single molecules to supramolecular assemblies," Trends in cell biology **25**, 730-748 (2015).
6. E. Betzig, "Single Molecules, Cells, and Super‐Resolution Optics (Nobel Lecture)," Angewandte Chemie International Edition **54**, 8034-8053 (2015).
7. W. E. Moerner, "Single‐Molecule Spectroscopy, Imaging, and Photocontrol: Foundations for Super‐Resolution Microscopy (Nobel Lecture)," Angewandte Chemie International Edition **54**, 8067-8093 (2015).
8. S. W. Hell, "Nanoscopy with focused light," Annalen der Physik **527**, 423-445 (2015).
9. T. Dertinger, R. Colyer, G. Iyer, S. Weiss, and J. Enderlein, "Fast, background-free, 3D super-resolution optical fluctuation imaging (SOFI)," Proceedings of the National Academy of Sciences **106**, 22287-22292 (2009).
10. T. Dertinger, M. Heilemann, R. Vogel, M. Sauer, and S. Weiss, "Superresolution optical fluctuation imaging with organic dyes," Angewandte Chemie **122**, 9631-9633 (2010).
11. P. Dedecker, G. C. Mo, T. Dertinger, and J. Zhang, "Widely accessible method for superresolution fluorescence imaging of living systems," Proceedings of the National Academy of Sciences **109**, 10909-10914 (2012).
12. X. Zhang, X. Chen, Z. Zeng, M. Zhang, Y. Sun, P. Xi, J. Peng, and P. Xu, "Development of a reversibly switchable fluorescent protein for super-resolution optical fluctuation imaging (SOFI)," ACS nano **9**, 2659-2667 (2015).
13. A. M. Chizhik, S. Stein, M. O. Dekaliuk, C. Battle, W. Li, A. Huss, M. Platen, I. A. Schaap, I. Gregor, and A. P. Demchenko, "Super-resolution optical fluctuation bio-imaging with dual-color carbon nanodots," Nano letters **16**, 237-242 (2015).
14. T. Dertinger, A. Pallaoro, G. Braun, S. Ly, T. A. Laurence, and S. Weiss, "Advances in superresolution optical fluctuation imaging (SOFI)," Quarterly reviews of biophysics **46**, 210-221 (2013).
15. S. Cho, J. Jang, C. Song, H. Lee, P. Ganesan, T.-Y. Yoon, M. W. Kim, M. C. Choi, H. Ihee, and W. Do Heo, "Simple super-resolution live-cell imaging based on diffusion-assisted Förster resonance energy transfer," Scientific reports **3**, 1208 (2013).
16. F. Hertel, G. C. Mo, S. Duwé, P. Dedecker, and J. Zhang, "RefSOFI for mapping nanoscale organization of protein-protein interactions in living cells," Cell reports **14**, 390-400 (2016).
17. L. Kisley, R. Brunetti, L. J. Tauzin, B. Shuang, X. Yi, A. W. Kirkeminde, D. A. Higgins, S. Weiss, and C. F. Landes, "Characterization of porous materials by fluorescence correlation spectroscopy super-resolution optical fluctuation imaging," ACS nano **9**, 9158-9166 (2015).
18. T. Dertinger, R. Colyer, R. Vogel, J. Enderlein, and S. Weiss, "Achieving increased resolution and more pixels with Superresolution Optical Fluctuation Imaging (SOFI)," Optics express **18**, 18875-18885 (2010).
19. S. Geissbuehler, N. L. Bocchio, C. Dellagiacoma, C. Berclaz, M. Leutenegger, and T. Lasser, "Mapping molecular statistics with balanced super-resolution optical fluctuation imaging (bSOFI)," Optical Nanoscopy **1**, 4 (2012).

20.   S. Jiang, Y. Zhang, H. Yang, Y. Xiao, X. Miao, R. Li, Y. Xu, and X. Zhang, "Enhanced SOFI algorithm achieved with modified optical fluctuating signal extraction," Optics express **24**, 3037-3045 (2016).

21.   H. Deschout, T. Lukes, A. Sharipov, D. Szlag, L. Feletti, W. Vandenberg, P. Dedecker, J. Hofkens, M. Leutenegger, and T. Lasser, "Complementarity of PALM and SOFI for super-resolution live-cell imaging of focal adhesions," Nature communications **7**, 13693 (2016).

22.   X. Yi, S. Son, R. Ando, A. Miyawaki, S. Weiss, "Moments reconstruction and local dynamic range compression of high order Super-resolution of Optical Fluctuation Imaging," doi: https://doi.org/10.1101/500819.

23.   M. G. Kendall, Alan Stuart, and J.K. Ord., *The advanced theory of statistics* (1968), Vol. 3.

24.   K. T. Shimizu, R. G. Neuhauser, C. A. Leatherdale, S. A. Empedocles, W. Woo, and M. G. Bawendi, "Blinking statistics in single semiconductor nanocrystal quantum dots," Physical Review B **63**, 205316 (2001).

25.   P. Charles, "Digital Video and HDTV Algorithms and Interfaces," Morgan Kaufmann Publishers, San Francisco, 260, 630 (2003).

26.   S. F. Gibson and F. Lanni, "Experimental test of an analytical model of aberration in an oil-immersion objective lens used in three-dimensional light microscopy," JOSA A **9**, 154-166 (1992).

27.   X. Yi, "SR_Simu3D" (2018), retrieved at https://xiyuyi.github.io/SR_simu3D/.

28.   Marcel Leutenegger, "Balanced super-resolution optical fluctuation imaging" (2012), retrieved at https://documents.epfl.ch/users/l/le/leuteneg/www/BalancedSOFI/index.html.